nature communications

Article

https://doi.org/10.1038/s41467-025-60950-8

Accelerating water dissociation to achieve ampere-level hydrogen peroxide electrosynthesis in brine and seawater

Received: 20 August 2024

Accepted: 10 June 2025

Published online: 01 July 2025

Check for updates

Jiahuan Nie[1,6], Qiao Jiang[1,6], Zhiyuan Sang[1,2], Min Zheng[3], Zhenxin Li[1], Wei Liu[1], De'an Yang[1], Yao Zheng[3], Lichang Yin[4], Feng Hou[1], Xiao Yan[5] & Ji Liang[1]

Ampere-level hydrogen peroxide (H_2O_2) electrosynthesis in brine and seawater via two-electron oxygen reduction reaction (2e$^-$ ORR) is promising, but limited by the slow water dissociation and insufficient protons in neutral media. Hence, we design a multifunctional $Ni(OH)_2$ nanoplates anchored on carbon nanotubes (CNTs) as 2e$^-$ ORR catalyst towards H_2O_2 electrosynthesis, where $Ni(OH)_2$ nanoplates accelerate water dissociation and proton transfer, resolving the critical proton shortage for H_2O_2 formation. Combined with exceptional chloride tolerance and suppressed hydrogen evolution, the catalyst achieves a high H_2O_2 yield of 141 mol g^{-1} h^{-1} (14.1 mmol cm^{-2} h^{-1}) at 1 A cm^{-2} and a long operation time over 150 h at 200 mA cm^{-2} in 1 M NaCl solution with >80% H_2O_2 selectivity. In natural seawater, it achieves a Faraday efficiency over 70% at 100 mA cm^{-2}. This work enables water purification/disinfection via simultaneous H_2O_2/active chlorine production, bridging electrosynthesis with environmental remediation.

Hydrogen peroxide (H_2O_2) is an important chemical, which has been widely used for various bleaching, sanitary, and ecological remediation purposes[1,2]. Unfortunately, the current H_2O_2 production is still dominated by the energy-intensive and centralized anthraquinone oxidation method, which is associated with significant transportation/storage risks and costs[3,4]. Considering this, the electrocatalytic two-electron oxygen reduction reaction (2e$^-$ ORR) has been regarded as a promising alternative due to its high safety, energy efficiency, eco-friendliness, and decentralized features[5,6]. Although great progress has been made for H_2O_2 production via the 2e$^-$ ORR under alkaline or acidic conditions recently, the significant difficulty in H_2O_2 separation from such electrolytes thus narrows down its application to very limited scenarios[7]. Consequently, developing a technology that can directly synthesize H_2O_2 in neutral conditions or even in natural water bodies without the requirement of post-synthesis separation is particularly attractive.

Brine, which mainly contains NaCl, is the most earth-abundant neutral medium and biocompatible with the human body. It has been identified as a primary research objective in the sustainable energy, biology, and environment-related fields[8]. The ever-increasing ecocrisis in relation to seawater pollution and eutrophication further signifies the necessity of direct H_2O_2 production in brine[9]. In addition, the coupled anodic chlorine evolution reaction (CER), when brine is used in the anode side of the electrolyzer, also generates value-added products, i.e., chlorine gas (Cl_2)[10], hypochlorous acid (HClO), and hypochlorite salts (ClO^-)[11], in which the ClO^-/HClO is another chemical for water purification/disinfection.

Unlike conventional acid or alkaline electrolytes, electrosynthesis of H_2O_2 via 2e$^-$ ORR in neutral brine is particularly sluggish and

---

[1]Key Laboratory of Advanced Ceramics and Machining Technology of Ministry of Education School of Materials Science and Engineering, Tianjin University, Tianjin, China. [2]School of Materials Science and Engineering, Peking University, Beijing, China. [3]School of Chemical Engineering, The University of Adelaide, Adelaide, SA, Australia. [4]Shenyang National Laboratory for Materials Science, Institute of Metal Research, Chinese Academy of Science, Shenyang, China. [5]Institute of Technology for Future Industry, Shenzhen Institute of Information Technology, Shenzhen, China. [6]These authors contributed equally: Jiahuan Nie, Qiao Jiang. e-mail: sangzhiyuan@tju.edu.cn; lcyin@imr.ac.cn; yanxiao@sziit.edu.cn; liangji@tju.edu.cn

unstable. On the one hand, neutral brine cannot provide enough protons on the absorbed O_2 to form *OOH[12], due to the sluggish water dissociation (WD) and the poor proton supply rate, collaboratively resulting in a significantly slower ORR kinetics and lower H_2O_2 yield rate than in acidic/alkaline electrolytes[13]. On the other hand, the chloride ions in salt water may be preferably adsorbed on the active sites and suppress the desired oxygen adsorption, thus compromising the ORR activity[14]. These characteristics thus impose significant challenges in developing high-efficiency and high-activity electrocatalysts for $2e^-$ ORR in neutral brine[6,7,15–17].

Interestingly, nickel hydroxide ($Ni(OH)_2$) possesses unique features that may tackle these two issues in one batch. Firstly, it already shows tolerance against the chloride-containing species, which has been proven in its excellent stability in brine electrocatalysis[18]. Secondly, this 3d transition metal hydroxide is also capable of catalytic water dissociation, proton generation, and their transportation, which may significantly reduce the energy barrier of the proton-involving processes, e.g., forming *OOH intermediate during $2e^-$ ORR. Moreover, $Ni(OH)_2$ has also been proven inactive for hydrogen evolution reaction (HER), potentially offering additional benefits for achieving high-rate H_2O_2 generation over a wide potential range (below 0 V vs. RHE) in brine[12,19].

On the basis of these considerations, we herein present a multifunctional $Ni(OH)_2$ nanoplates anchored on carbon nanotubes (CNTs) for $2e^-$ ORR in neutral brine. The unsaturated coordination Ni atoms exposed on O-vacancies or at the edge over the $Ni(OH)_2$ nanoplates act as the major active sites for $2e^-$ ORR electrocatalysis[20,21], while the CNTs improve the electronic conductivity (Fig. 1). These merits, together with its suppression of hydrogen evolution, collaboratively result in a high H_2O_2 selectivity of over 85% in a wide potential range of 0.3 to −1.0 V vs. RHE, a high H_2O_2 yield rate of $30.86 \pm 0.03\ mol\ g^{-1}\ h^{-1}$ ($3.086\ mmol\ cm^{-2}\ h^{-1}$) at $200\ mA\ cm^{-2}$ and $141\ mol\ g^{-1}\ h^{-1}$ ($14.1\ mmol\ cm^{-2}\ h^{-1}$) at $1\ A\ cm^{-2}$, and operational stability of over 156 h at $200\ mA\ cm^{-2}$ with a high FE over 80%. Even in natural seawater, this catalyst still shows an excellent electrocatalytic performance with a H_2O_2 yield of $14.2\ mol\ g^{-1}\ h^{-1}$ ($1.42\ mmol\ cm^{-2}\ h^{-1}$) at $100\ mA\ cm^{-2}$ with FE over 70%. In a prototype electrolyzer with our catalyst, the electrosynthesized H_2O_2 demonstrates rapid water treatment and disinfection capability. This study proves the feasibility of the electrosynthesis H_2O_2 in seawater coupled with the CER in the anodic tank with extra valuable industrial chemicals production, i.e., ClO^- disinfectants, which endows it huge potential in practical application, i.e., to alleviate seawater pollution.

Results

Theoretical prediction guided material synthesis

Firstly, density functional theory (DFT) calculations were performed to confirm the intrinsic capability of $Ni(OH)_2$ for ORR in brine. The adsorption free energy of the key *OOH intermediates (ΔG_{*OOH}) at the exposed Ni sites was calculated to be 4.14 eV, which is very close to the ideal value of ΔG_{*OOH} (4.23 eV) for $2e^-$ ORR. It corresponds to a small overpotential of only 0.09 eV, indicating its nearly barrier-free $2e^-$ ORR activity (Fig. 2a, Supplementary Fig. 1 and Supplementary Data 1). As for the comparative Ni sites in NiO, they show a lower ΔG_{*OOH} value of 3.06 eV, which is far from the ideal value, corresponding to a huge overpotential of 1.17 eV for $2e^-$ ORR and indicating its preferred $4e^-$ pathway for ORR. (and the activation barrier of *OOH formation on the active sites of NiO and $Ni(OH)_2$ will be discussed later). To illustrate the chlorine resistance capability of $Ni(OH)_2$ in seawater, we conducted 5 ns molecular dynamics simulations using the large-scale atomic/molecular massively parallel simulator (LAMMPS). As shown in Fig. 2b and Supplementary Data 1, during the simulation process after reaching equilibrium under different electric fields, the distribution of chloride ions on the surface of the material was rather sparse, with a concentration not exceeding $0.1\ g\ cm^{-3}$. Compared with Ni and NiO, there were fewer chloride ions on the surface of the material due to the repulsion of OH groups (Supplementary Fig. 2 and Supplementary Data 1), which demonstrated the better chlorine resistance performance of $Ni(OH)_2$. In addition, the optimized models for H* adsorption on Ni sites also show

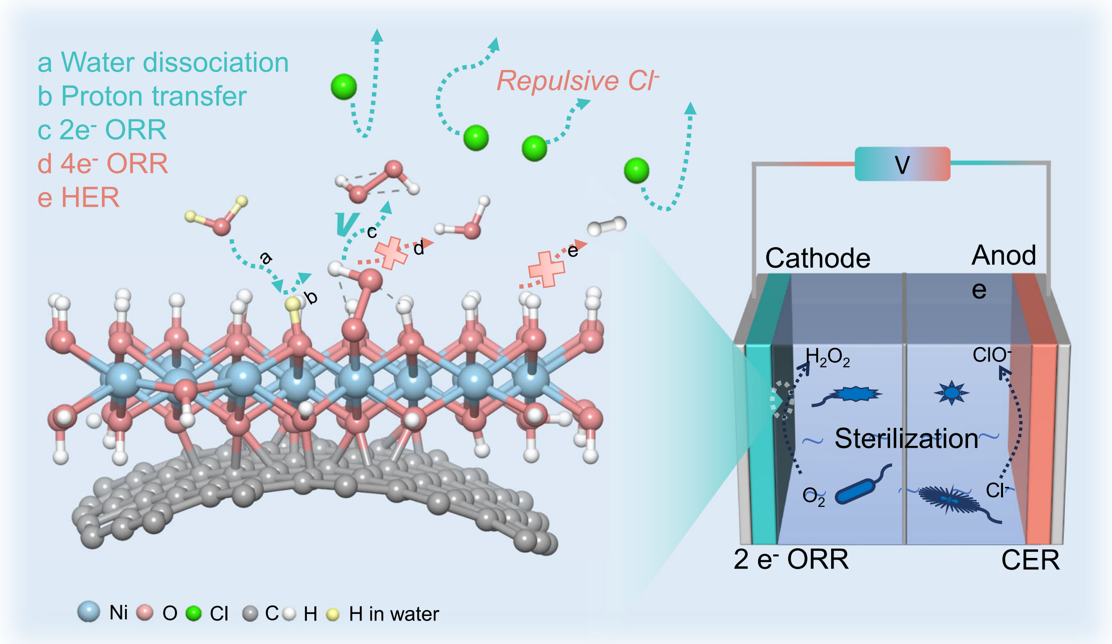

Fig. 1 | Illustration of the advantages of $Ni(OH)_2$/CNT to selective H_2O_2 electrosynthesis, and the possible tanks with $2e^-$ ORR and CER. Schematic diagram on the proton transfer and water dissociation of $Ni(OH)_2$ to rapid *OOH formation, and the undesirable $4e^-$ ORR and hydrogen evolution process in neutral environment over $Ni(OH)_2$/CNT (left); Schematic diagram on the tanks with $2e^-$ ORR coupled with the CER reaction in the anodic tank (right).

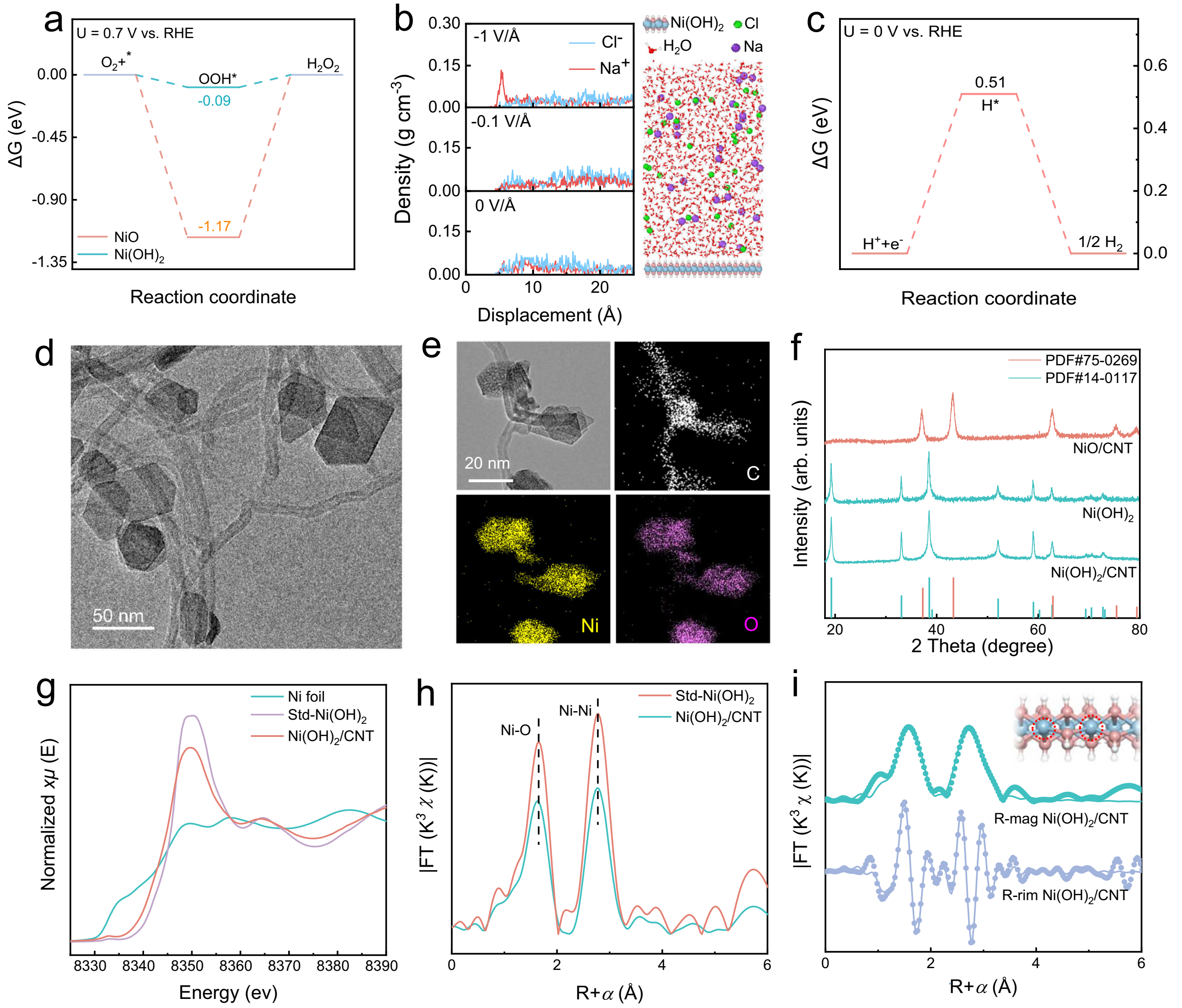

Fig. 2 | Theoretical prediction guided $Ni(OH)_2$/CNT synthesis and the structural characterizations. **a** Gibbs free energy diagram for 2e⁻ ORR at 0.7 V vs. RHE. **b** The density distributions of chloride ions in the z-axis direction for $Ni(OH)_2$ (left) and equilibrium configuration of electrolyte system (3.6 wt% NaCl) above the electrode surface of $Ni(OH)_2$, viewed from XZ cross-section. **c** Calculated free energy diagram for HER on $Ni(OH)_2$. **d** The TEM image of $Ni(OH)_2$/CNT. **e** STEM image of $Ni(OH)_2$/CNT and corresponding elemental mapping images of Ni, C and O. **f** XRD pattern of $Ni(OH)_2$/CNT, $Ni(OH)_2$ and NiO/CNT. **g** Ni *K*-edge XANES of $Ni(OH)_2$/CNT, standard $Ni(OH)_2$ and Ni foil. **h** Ni *K*-edge EXAFS-FT signals of $Ni(OH)_2$/CNT and standard $Ni(OH)_2$. **i** EXAFS fitting results using the model with a path of Ni-O and Ni-Ni in *R* space (FT magnitude and imaginary part). The k^3-weighted and not phase-corrected. The blue, pink and white represent nickel, oxygen and hydrogen, respectively.

that hydrogen adsorption is weak on the surface of $Ni(OH)_2$ with an expected large overpotential of ~0.51 eV for HER (Fig. 2c). Meanwhile, the large kinetic barrier of *H absorbed at the Ni site also confirms its inactiveness for catalyzing HER (Supplementary Fig. 3), enabling the possible 2e⁻ ORR at negative potentials below 0 V vs. RHE to achieve a high H_2O_2 yield rate.

Based on these predictions, $Ni(OH)_2$ nanoplates, exposed sufficient surface and edge Ni sites, were grown on CNTs via a simple hydrothermal process. Transmission electron microscopy (TEM) images show that the $Ni(OH)_2$ nanoplates, with a typical two-dimensional structure of 20–50 nm, are attached to CNTs (Fig. 2d). Meanwhile, the pure $Ni(OH)_2$ and NiO/CNT are also prepared for comparison, which also possess a well-distributed and 2D nanoplate morphology (Supplementary Fig. 4). Under high resolutions, the lattice fringes show a planar spacing of 0.236 nm, which can be ascribed to the (101) facet of $Ni(OH)_2$ (Supplementary Fig. 5), confirming the successful formation of β-$Ni(OH)_2$. Meanwhile, the obvious lattice fringe of 0.209 nm and 0.240 nm can be ascribed to the (200) facet of NiO/CNT and the (101) facet of $Ni(OH)_2$[22,23], respectively (Supplementary Figs. 6 and 7). The energy-dispersive X-ray spectroscopy (EDS) elemental mappings present the distribution of Ni, O, and C elements, respectively conformal with the $Ni(OH)_2$ nanoplates and CNTs (Fig. 2e). The X-ray diffraction (XRD) patterns confirm the formation of β-$Ni(OH)_2$ phase in $Ni(OH)_2$/CNT, similar to the sole $Ni(OH)_2$ nanoplates without CNTs (Fig. 2f)[22] and in agreement with the TEM observations. In addition, the obvious electron paramagnetic resonance (EPR) signals for the $Ni(OH)_2$/CNT, NiO/CNT, and $Ni(OH)_2$ indicate the existence of O vacancies trapped with extra electrons (Supplementary Fig. 8)[24], which would improve the number of exposed Ni sites at the O vacancies for ORR electrocatalysis.

To probe the chemical structure of the materials, X-ray photoelectron spectroscopy (XPS) was carried out. As shown in Supplementary Figs. 9 and 10, the survey scan confirms the coexistence of Ni and O for $Ni(OH)_2$/CNT and NiO/CNT[25]. For the Ni 2*p* spectra in

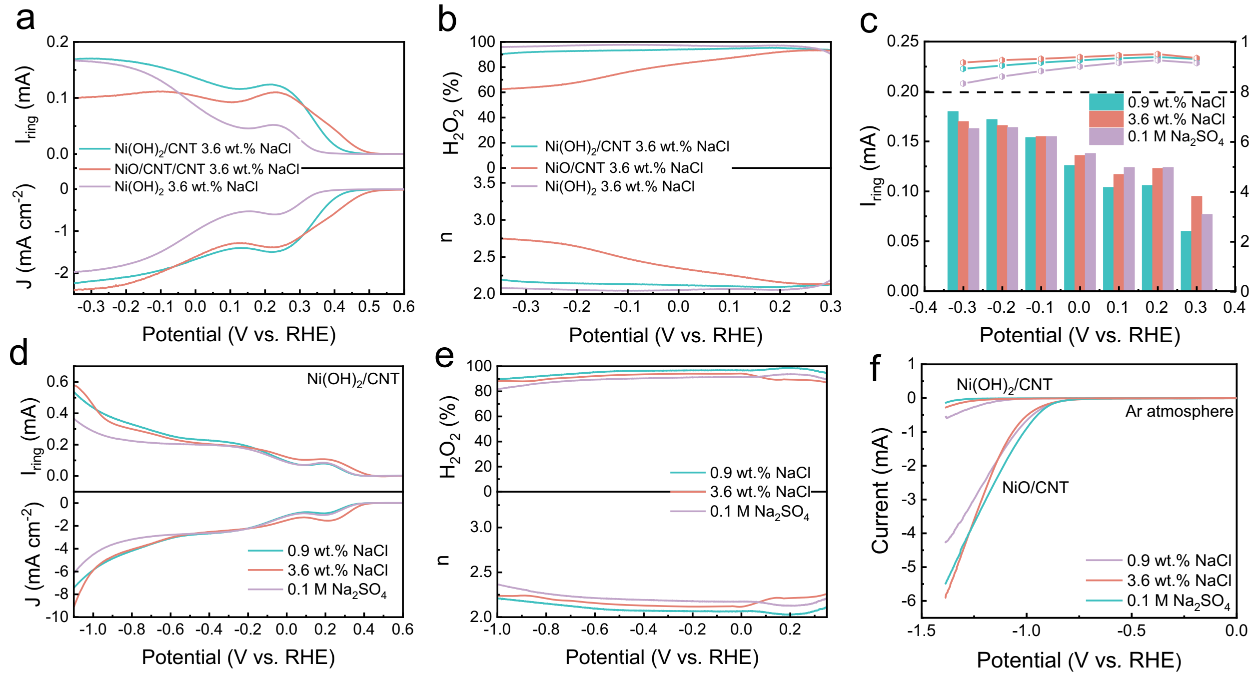

Fig. 3 | Electrochemical 2e$^-$ ORR catalytic performance of Ni(OH)$_2$/CNT. a LSV curves of different samples, tested at 1600 rpm and a rate of 10.0 mV s^{-1}, showing a the current (densities) on the disk (j_{disk}) and ring (I_{ring}) electrodes and **b** H$_2$O$_2$ selectivity and electron number of the materials in 3.6 wt. % NaCl. **c** Comparison of I_{ring} and selectivity of Ni(OH)$_2$/CNT in 0.9 wt. % NaCl, 3.6 wt. % NaCl and 0.1 M Na$_2$SO$_4$. **d** LSV and **e** H$_2$O$_2$ selectivity and electron number of Ni(OH)$_2$/CNT at wide potential range. **f** Polarization curves of Ni(OH)$_2$/CNT and NiO/CNT in Ar-saturated neutral electrolyte.

Ni(OH)$_2$/CNT, it can be deconvolved into Ni^{2+} 2$p_{3/2}$ species at 855.58 eV and a Ni^{2+} 2$p_{1/2}$ species at 873.22 eV[26], slightly shifted to a higher binding energy compared with Ni(OH)$_2$ (855.28 vs. 872.92 eV), indicating there is a charge transfer from Ni(OH)$_2$ to the oxygen-containing functional groups in Ni(OH)$_2$/CNT[27]. However, there is no obvious effect on the performance of 2e$^-$ ORR in Ni(OH)$_2$/CNT, because the major active sites are the unsaturated coordination Ni atoms exposed on O-vacancies or at the edge over the Ni(OH)$_2$ nanoplates[20,21] rather than the Ni sites close to CNTs.

X-ray absorption spectroscopy (XAS), including X-ray absorption near-edge structure (XANES) and extended X-ray absorption fine structure (EXAFS) measurements, was then carried out to clarify the coordination environment of the Ni sites in Ni(OH)$_2$/CNT and NiO/CNT (Supplementary Figs. 11 and 12). The absorption edge of Ni *K*-edge XANES of Ni(OH)$_2$/CNT and NiO/CNT is slightly red-shifted in comparison with the standard Ni(OH)$_2$ and NiO sample (Fig. 2g), which may be caused by oxygen vacancies[28]. Meanwhile, in the Fourier transform EXAFS spectra of Ni(OH)$_2$/CNT and the comparative Ni(OH)$_2$, they both exhibit a main peak at 1.66 Å corresponding to the Ni-O species and a secondary peak at 2.69 Å corresponding to the Ni-Ni species[29] (Fig. 2h), which indicates their similar Ni-O coordination configurations. Of note, the intensities of the Ni-O and Ni-Ni peaks of Ni(OH)$_2$/CNT are considerably lower than those of the standard Ni(OH)$_2$ sample, again suggesting the existence of structural defects in it[30]. The EXAFS fitting results confirm that the number of O atoms in the first coordination shell of the Ni sites is 5.7 (i.e., Ni-O$_{5.7}$) with a distance of 2.07 Å (Fig. 2i and Supplementary Table 1), which also confirms the existence of O vacancies in Ni(OH)$_2$/CNT, and the exposed unsaturated Ni atoms on these sites would be the potential active sites for 2e$^-$ ORR electrocatalysis.

Electrocatalytic performance for 2e$^-$ ORR under brine

The electrocatalytic 2e$^-$ ORR performance of the material was first evaluated in 3.6 wt% NaCl aqueous solution (i.e., simulated seawater) by linear sweep voltammetry (LSV) on a rotating ring-disk electrode, in which the collection coefficient is 0.37 (Fig. 3a and Supplementary Fig. 13). Ni(OH)$_2$/CNT delivers the largest ring current, indicating its favorable two-electron pathway for ORR and the excellent chloride-tolerating capacity. Correspondingly, it possesses a high H$_2$O$_2$ selectivity of over 90% (Fig. 3b). Besides, the pure Ni(OH)$_2$ also maintains the high H$_2$O$_2$ selectivity but with much lower current densities on both the disk and ring compared with Ni(OH)$_2$/CNT. This confirms that the major role of introducing CNTs is to facilitate the reaction kinetics by significantly enhancing the electronic conductivity of the catalyst, while the intrinsic capability of Ni(OH)$_2$ for highly selective 2e$^-$ ORR catalysis can be fully exploited in this case for Ni(OH)$_2$/CNT (Supplementary Fig. 14).

In addition, either in diluted NaCl solution (0.9 wt% NaCl solutions, i.e., physiological saline), or in the 0.1 M Na$_2$SO$_4$ solution, the Ni(OH)$_2$/CNT material both shows high ORR current densities and H$_2$O$_2$ selectivity of over 80% (Fig. 3c). Similarly, Ni(OH)$_2$/CNT also shows excellent 2e$^-$ ORR selectivity in other electrolytes, such as 0.1 M KOH (FE = 94%), simulated alkaline seawater (3.6 wt% NaCl + 0.1 M KOH, FE = 96%), natural seawater from Bohai Sea (FE = 80%), and alkaline seawater (natural seawater + 0.1 M KOH, FE = 85%) (Supplementary Figs. 15 and 16), which further confirms the huge potential of the H$_2$O$_2$ electrosynthesis using this Ni(OH)$_2$/CNT material and its applicational readiness in various practical conditions.

In addition to the aforementioned merits, Ni(OH)$_2$/CNT also shows stable current plateaus on both the ring and disk electrodes till as negative as −1.0 V vs. RHE, with stably high H$_2$O$_2$ selectivity up to 98% in the O$_2$-saturated neutral electrolyte (3.6 wt% NaCl, 0.9 wt% NaCl, and 0.1 M Na$_2$SO$_4$) (Fig. 3d, e). Such stable 2e$^-$ ORR performance at low potentials, which is rarely achieved previously, clearly confirms the superiority of the material for selectively catalyzing 2e$^-$ ORR and suppressing HER. This is further proven by the fact that Ni(OH)$_2$/CNT exhibits a high overpotential of over 1.0 V for the HER in all neutral media, according to the LSV curves in the Ar atmosphere (Fig. 3f), which is also consistent with the DFT results (Fig. 2c)[31]. In addition, Ni(OH)$_2$/CNT also showed low catalytic activity towards H$_2$O$_2$

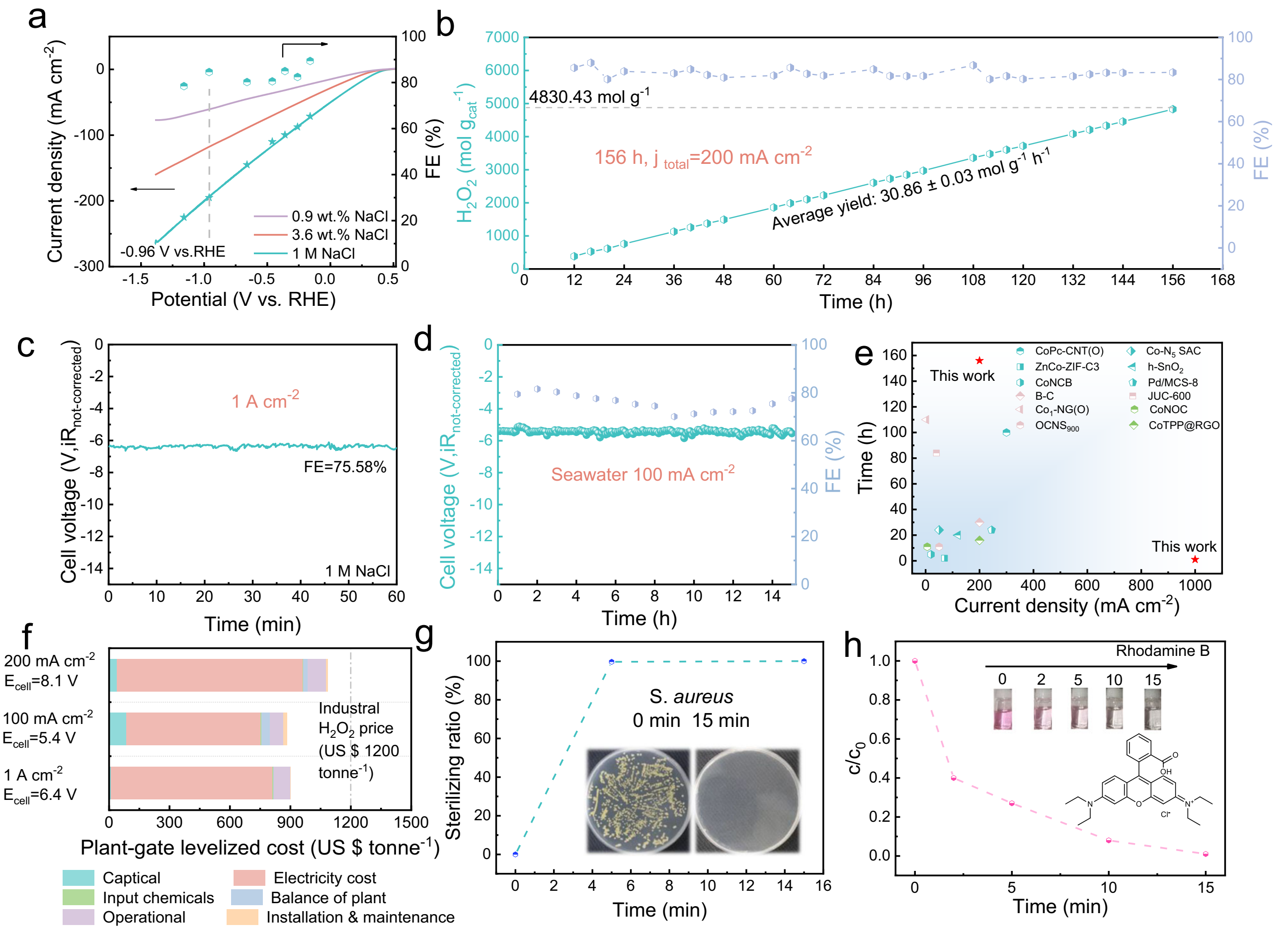

Fig. 4 | H_2O_2 production performance of $Ni(OH)_2$/CNT materials in the flow cell. **a** LSV polarization curve of $Ni(OH)_2$/CNT in different concentration NaCl solutions and FE of $Ni(OH)_2$/CNT in 1 M NaCl. **b** FE and linear fitted lines for the accumulation of H_2O_2 yields in 1 M NaCl for 156 h electrolysis. **c** The stability test of $Ni(OH)_2$/CNT at 1 A cm^{-2} in 1 M NaCl. **d** The stability test of $Ni(OH)_2$/CNT tested in natural seawater from Bohai Sea. **e** A comparison of stability reported with the most advanced electrocatalysts newly reported under various electrolysis configurations (cyan symbols: neutral electrolyte; pink symbols: alkaline electrolyte; green symbols: acid electrolyte. CoPc-CNT(O)[27], Co-N_5 SAC[65], ZnCo-ZIF-C3[66], h-SnO_2[29], CoNCB[67], Pd/MCS-8[68], B-C[69], JUC-600[70], $OCNS_{900}$[71], Co_1-NGO[34], CoNOC[37], CoTPP@RGO[72], Data sources are provided in Table S2). **f** Techno-economic analysis of H_2O_2 electrosynthesis with three different conditions. **g** Bactericidal rate of *S. aureus* in 0.9 wt.% NaCl. **h** UV-vis spectra during the decomposition process of Rhodamine B.

reduction reaction (H_2O_2RR, Supplementary Fig. 17) as well as the smallest Tafel slope (82.94 mV dec^{-1}) among the three samples (Supplementary Fig. 18). These unique features of the material further guarantee its feasibility to be used at high overpotentials for achieving high-rate H_2O_2 generation while maintaining a high efficiency simultaneously.

H_2O_2 production performance in flow cells and applicational perspectives

A homemade prototype electrolyzer was subsequently constructed to evaluate the ORR-to-H_2O_2 performance of $Ni(OH)_2$/CNT in neutral electrolytes for long-term operation. In this electrolyzer, $Ni(OH)_2$/CNT was coated on a carbon paper with a gas-diffusion layer (GDL, SGL-39BB) and was used as the working electrode. Ag/AgCl and Ru/Ir-coated Ti mesh were used as the reference electrode and counter electrode. A Nafion film (117) was used as the separator (Supplementary Fig. 19). The accumulated H_2O_2 concentration in the electrolyte was quantified by the potassium oxalate colorimetric method according to the standard curve in Supplementary Fig. 20. In 1 M NaCl electrolyte, $Ni(OH)_2$/CNT delivers a high FE of over 80% with increasing ORR current densities until 200 mA cm^{-2}. In other electrolytes with lower NaCl concentrations, including 3.6 wt% NaCl (simulated seawater) and 0.9 wt% NaCl (physiological saline), the ORR current density could still exceed 100 and 50 mA cm^{-2} while maintaining a high Faraday efficiency of over 80% until −0.96 V vs. RHE, respectively (Fig. 4a and Supplementary Fig. 19a). Correspondingly, high H_2O_2 yields of 30, 18 and 10.86 mol g^{-1} h^{-1} (3, 1.8, 1.086 mmol cm^{-2} h^{-1}) were achieved in 1 M NaCl, 3.6 wt% NaCl and 0.9 wt% NaCl electrolytes (Supplementary Fig. 21), respectively. In addition, $Ni(OH)_2$/CNT also exhibits a high yield of 18.71 mol g^{-1} h^{-1} (1.871 mmol cm^{-2} h^{-1}) at 100 mA cm^{-2} with FE of 80% at −0.96 V vs. RHE in 0.5 M Na_2SO_4 electrolyte (Supplementary Fig. 22). Besides, $Ni(OH)_2$/CNT also has high yield in alkaline electrolyte (Supplementary Fig. 19a and Supplementary Figs. 23). These solidly validate the practical feasibility of electrocatalytic H_2O_2 synthesis under various conditions.

The electrochemical stability of $Ni(OH)_2$/CNT was examined at a constant current density of 200 mA cm^{-2}. The FE of $Ni(OH)_2$/CNT maintained over 80% during the whole 156 h testing period, with an average apparent H_2O_2 yield rate of 30.86 ± 0.03 mol g^{-1} h^{-1} (3.086 mmol cm^{-2} h^{-1}), corresponding to a specific H_2O_2 yield up to 4830.43 mol g$_{cat}^{-1}$ during the whole test (Fig. 4b and Supplementary Figs. 19a and 24). Besides, as shown in Supplementary Figs. 25-27, the SEM, XRD, and XPS results of $Ni(OH)_2$/CNT show that the morphology and structure of $Ni(OH)_2$/CNT remain intact after the 100 h i-t test at 200 mA cm^{-2} in 1 M NaCl electrolyte, which indicates that $Ni(OH)_2$/CNT structure is fairly stable. More importantly, at a high current density of

1 A cm^{-2}, $Ni(OH)_2$/CNT delivers a high H_2O_2 yield of 141 mol g^{-1} h^{-1} (14.1 mmol cm^{-2} h^{-1}, FE = 75.58%) and a cell voltage (E_{cell}) of 6.4 V (non-iR-corrected)[27] was required (Fig. 4c and Supplementary Figs. 19b and 28). This high current density dominates among state-of-the-art electrocatalysts for 2e$^-$ ORR (Supplementary Table 2). Moreover, in the natural seawater from Bohai Sea, $Ni(OH)_2$/CNT also shows excellent electrochemical properties considering the high H_2O_2 yield of 14.2 mol g^{-1} h^{-1} (1.42 mmol cm^{-2} h^{-1}) at 100 mA cm^{-2} with FE over 70% (Fig. 4d and Supplementary Fig. 29). In this test, 1 M H_3PO_4 is used as the anolyte to prevent the formation of precipitate in the seawater during the reaction (Supplementary Fig. 19c). Besides, $Ni(OH)_2$/CNT has higher H_2O_2 yield (30 mol g^{-1} h^{-1}) and FE (>80%) in 1 M NaCl compared with NiO/CNT (12.3 mol g^{-1} h^{-1}, 50%), which highlights the excellent performance of $Ni(OH)_2$/CNT (Supplementary Figs. 19a and 30). In addition, the stability of the material, tested at 200 mA cm^{-2} and 1 A cm^{-2}, surpasses most of the recently published catalysts for electro-producing H_2O_2 (Fig. 4e and Supplementary Table 2), which clearly demonstrates the superiority of this material.

Techno-economic analysis was further conducted in flow cell to estimate the plant-gate levelized cost for H_2O_2 production using $Ni(OH)_2$/CNT at current densities of 1 A cm^{-2} (US \$901 tonne^{-1}) and 200 mA cm^{-2} (US\$1085.65 tonne^{-1}) in 1 M NaCl and 100 mA cm^{-2} (US \$882.77 tonne^{-1}) in natural seawater, both of which are lower than the market price of H_2O_2[27,32] (US\$ 1200 tonne^{-1}, Fig. 4f, Supplementary Fig. 31, Supplementary Notes 1 and 2 contain details of parameters and calculation processes used in economic analyzes), which can be mainly attributed to its zero separation cost, cheap raw materials, and readiness for scaling up (Supplementary Fig. 32).

The unique feature of this technology endows it with significant feasibility for practical applications, including disinfection and wastewater treatment, etc. To verify this, *S. aureus* was selected, and it was shown that this technology can effectively eliminate *S. aureus* in 0.9 wt % NaCl solution after only 5 min of H_2O_2 electrosynthesis, with a 99.99% sterilizing ratio (Fig. 4g, Supplementary Fig. 33 and Supplementary Table 3). In addition, 1 M NaCl solution after 20 min of H_2O_2 electrosynthesis at 200 mA cm^{-2} can be directly utilized as a Fenton reagent under sunlight irradiation, which can effectively eliminate *Rhodamine B* in 15 min and *Methylene Blue* in 90 min (Fig. 4h, Supplementary Figs. 34 and 35), demonstrating the effectiveness of generated H_2O_2 for water treatment and disinfection[33].

Of note, when NaCl solution was used for both electrodes, the anodic half-reaction was the dominant chlorine evolution reaction (CER), rather than the common oxygen evolution reaction, which was confirmed by the lower onset potential and large current density of Ru/Ir-coated Ti mesh anode in the NaCl solutions than that of in Na_2SO_4 solutions from the anodic LSV curves (Supplementary Fig. 36). In addition, the CER process would also generate value-added products, i.e., chlorine gas (Cl_2), hypochlorous acid (HClO), and hypochlorite salts (ClO^-), in which the ClO^-/HClO is the major product of CER in brine and is another chemical for water purification/disinfection. To prove this, anolyte running at 200 mA cm^{-2} could oxidize the I^- ions into I_2, thus changing the transparent NaI solution into a dark yellow color (Supplementary Fig. 37), confirming the generation of ClO^-. The 2e$^-$ ORR towards H_2O_2 production, coupled with the anodic CER reactions, would more effectively produce disinfectants and provide a possible method to alleviate serious marine pollution.

An original mechanism for 2e$^-$ ORR: the water dissociation and proton transfer in $Ni(OH)_2$/CNT

Apart from tailoring the electronic structure of the catalysts to alter *OOH intermediates adsorption to achieve high ORR activity and H_2O_2 selectivity[34], as previously calculated in a thermodynamics aspect (Fig. 2a), the kinetics of the *OOH intermediate formation is another key factor in 2e$^-$ ORR towards high-rate H_2O_2 electrosynthesis, which has often been neglected. The formation rate of *OOH intermediates depends on the proton supply rate. To further explore the 2e$^-$ ORR process in $Ni(OH)_2$/CNT, DFT calculations were performed to obtain the kinetic barrier of proton transfer and water dissociation.

As shown in Fig. 5a, the kinetic barrier of proton migration via hydroxyl groups on $Ni(OH)_2$ to the adjacent adsorbed oxygen molecules was calculated to be 0.35 eV at 0.7 V vs. RHE (the equilibrium potential of H_2O_2). When the applied potential was reduced to 0.5 V vs. RHE, the proton transfer barrier further decreased to 0.12 eV, indicating a highly facile proton transfer on our material (Supplementary Fig. 38 and Supplementary Data 1). However, the kinetic barrier of proton migration from H_2O in NiO at 0.7 V vs. RHE was calculated to be 1.21 eV (Supplementary Fig. 39), much higher than that of $Ni(OH)_2$/CNT (0.35 eV), indicating that efficient proton transfer from nearby hydroxy groups to the absorbed O_2 can thus reduce the formation energy of intermediate *OOH as well. Besides, the energy barriers of water dissociation on $Ni(OH)_2$ surface were calculated to be 0.44 eV (Supplementary Fig. 40 and Supplementary Data 1). In 2e$^-$ ORR process, OOH is formed when O_2 adsorbed at unsaturated Ni sites attracts nearby hydrogen from hydroxy groups, Ni-O sites were exposed when the hydroxy hydrogen was consumed. Then, the OH group and H atom in the H_2O molecule were attracted by the unsaturated Ni sites and Ni-O sites on $Ni(OH)_2$/CNT, respectively. This simultaneous absorption of O and H atoms in the water molecule destabilizes the H-OH bond[23], which would greatly facilitate the dissociation of water[30]. Meanwhile, Ni-OH reforms due to the Ni-O site traps hydrogen and Ni-OH$^-$ forms due to the Ni sites traps OH from water molecule, respectively. The Ni-OH species can provide sufficient proton supply for catalytic oxygen reduction, which accelerates the protonation of absorbed O_2 to form *OOH species during ORR, in a streamline manner (Fig. 5b and Supplementary Data 1). Subsequently, the OH$^-$ at Ni-OH$^-$ strips off into the electrolyte because of the repulsive effect of negative potential applied to cathode[30,35], which recombines with a proton from the anode side to form a water molecule. In this regard, continuous proton generation and their migration to the absorbed O_2 molecules can be achieved, which is favorable for the *OOH formation and subsequent H_2O_2 formation[17].

In addition, avoiding the cleavage of O-O bond in the adsorbed *OOH intermediate is another important requirement for H_2O_2 generation via 2e$^-$ ORR[36]. Therefore, the kinetic barriers of *OOH protonation for 2e$^-$ ORR pathway ($*OOH + H \rightarrow H_2O_2$) and *OOH dissociation for 4e$^-$ ORR pathway ($*OOH + H \rightarrow *O + H_2O$)[16,37] over $Ni(OH)_2$ surface were calculated to better understand the origin of the excellent selectivity of H_2O_2 electrosynthesis. For the 2e$^-$ ORR pathway, $Ni(OH)_2$ shows low kinetic barriers of 0.46 and 0.58 eV at 0.5 and 0.7 V vs. RHE (described by the Ni-O_2 bond elongation until breaking), respectively. For the 4e$^-$ ORR pathway to produce H_2O (described by the O-O bond elongation until breaking in *OOH intermediate), however, obviously higher kinetic barriers of 0.65 and 0.73 eV at 0.5 and 0.7 V vs. RHE were obtained, respectively (Supplementary Fig. 41 and Supplementary Data 1). It thus indicates the binding of the O-O bond is stronger than that of the Ni-O bond, allowing the key *OOH intermediate to be well reserved for forming H_2O_2. It also clearly confirms the advantages of $Ni(OH)_2$ in stabilizing O_2* adsorbents and preventing the over-protonation of OOH* intermediates, thereby leading to a highly selective and rapid H_2O_2 production[38,39].

To verify these simulation results, in-situ attenuated total reflectance surface-enhanced infrared absorption spectroscopy (ATR-SEIRAS) and ex-situ Fourier transform infrared spectroscopy (FTIR) were performed for $Ni(OH)_2$/CNT and NiO/CNT[40]. As shown in Fig. 5c, both materials exhibit peaks at 1120 and 1450 cm^{-1} from 0.5 V to 0 V vs. RHE during the ORR process, and these two prominent peaks could be assigned to the surface-adsorbed OOH (*OOH) and O_2 species[41–43], respectively. It is clear that the intensities of the peak at 1450 cm^{-1} (i.e., adsorbed O_2) for both samples are comparable, while the intensities at

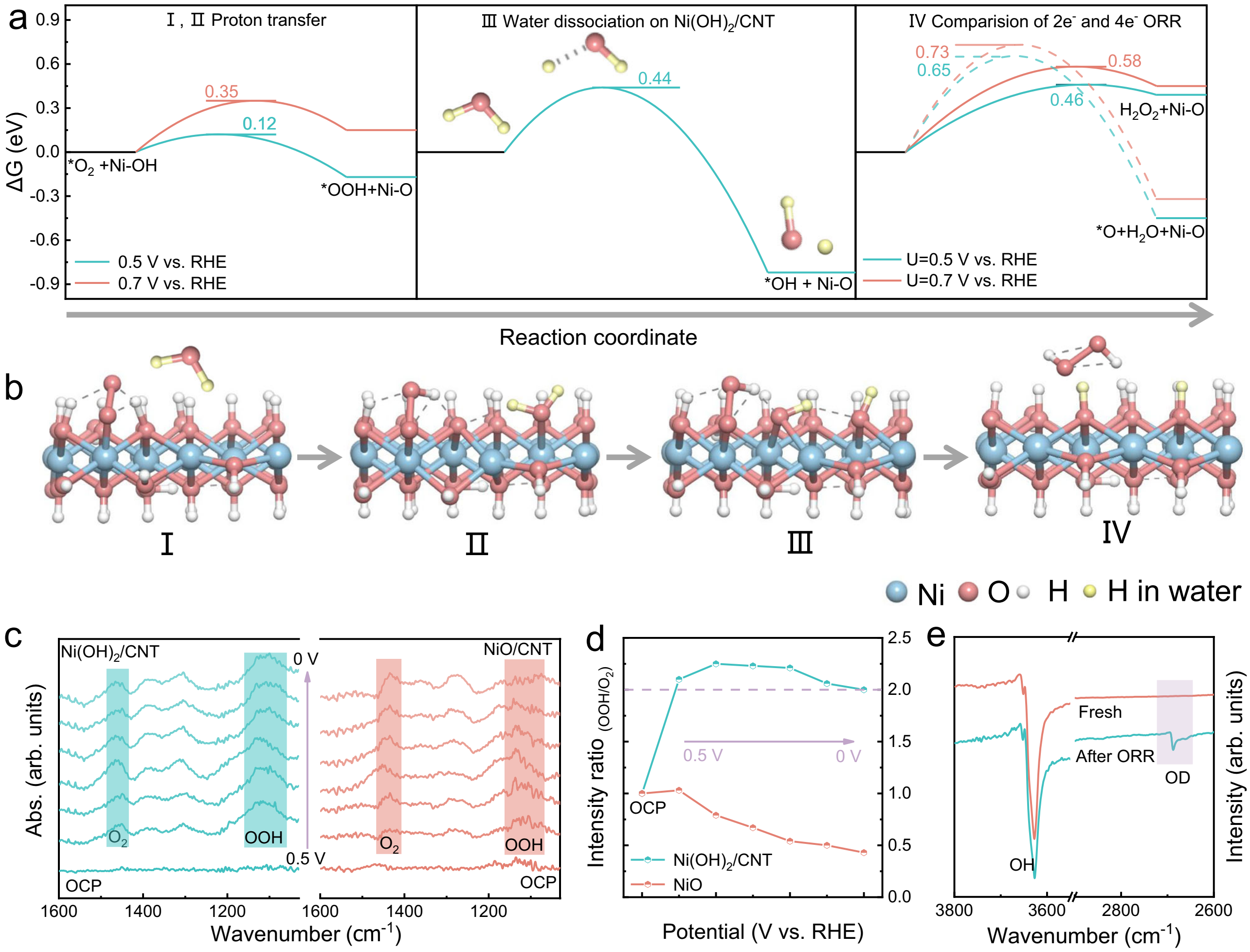

Fig. 5 | Theoretical insight for excellent ORR performances. DFT calculations of the $Ni(OH)_2$ interface. **a** I, Proton transfer (PT) at U = 0.5 V vs. RHE and U = 0.7 V vs. RHE. II, III, Water dissociation process on the outer surface of $Ni(OH)_2$ and the optimized geometries of the initial, transition and final state. IV, *OOH protonation for $2e^-$ ORR pathway (*OOH + H→H_2O_2, solid line) and *OOH dissociation for $4e^-$ ORR pathway (*OOH + H→*O + H_2O, dotted line) of Ni(OH) at U = 0.5 V and U = 0.7 V vs. RHE. The pink and yellow represent oxygen and hydrogen in water, respectively. **b** The optimized structure of ORR process. The blue, pink, white and yellow represent nickel, oxygen in $Ni(OH)_2$ and hydrogen in $Ni(OH)_2$ and H in water, respectively. **c** In situ ATR-SEIRAS spectra for $Ni(OH)_2$/CNT and NiO/CNT at different potentials in O_2-saturated 3.6 wt. % NaCl solution. **d** Intensity ratio of OOH and O_2 from ATR-SEIRAS. **e** FT-IR spectra of $Ni(OH)_2$/CNT before and after oxygen reduction reaction, respectively.

1120 cm^{-1} (i.e., adsorbed OOH) for $Ni(OH)_2$/CNT are much higher than that for NiO/CNT at all testing potentials (Fig. 5d), indicating the higher *OOH formation rate on $Ni(OH)_2$/CNT[44,45]. This result agrees well with the above simulation conclusions that the efficient proton transfer and water dissociation accelerate the formation of *OOH intermediates. Besides, ex-situ FTIR further elucidates the role of $Ni(OH)_2$ as proton donors, which was conducted after ORR in the O_2-saturated 3.6 wt% NaCl D_2O solution. As shown in Fig. 5e, a new peak occurs at 2600–2700 cm^{-1}, which can be attributed to the OD groups[46], confirming that the H atoms in the hydroxy groups of $Ni(OH)_2$ have been partially replaced by D atoms from the dissociation of D_2O. It thus can be deduced that the protons obtained from water dissociation supplement the protons in the hydroxy group in $Ni(OH)_2$, which was consumed for the protonation of absorbed O_2 to OOH species during ORR, in a pipeline manner, as shown in path a–c in Fig. 1. This accelerates the formation of *OOH intermediates and is conducive to achieving a rapid H_2O_2 electrosynthesis.

Discussion

In this work, we present a $Ni(OH)_2$-based catalyst with $Ni(OH)_2$ nanoplates grown on carbon nanotubes for efficient and rapid H_2O_2 electrosynthesis in salt water. In this material, $Ni(OH)_2$ shows a unique capability of swift proton transfer and rapid water dissociation, even under neutral conditions, ensuring a sufficient proton supply to the Ni active sites for rapid *OOH formation and H_2O_2 generation. Meanwhile, the strong inhibition against the undesirable $4e^-$ ORR/HER and excellent chloride resistance of the material collaboratively guarantee a high $2e^-$ ORR selectivity in Cl^--containing brine. Consequently, the as-prepared $Ni(OH)_2$/CNT exhibits a high H_2O_2 selectivity consistently exceeding 85% in salt water over a wide potential range of −1 to 0.3 V vs. RHE. In 1 M NaCl electrolyte, it exhibits high H_2O_2 yield rate (30.86 mol g^{-1} h^{-1} @ 200 mA cm^{-2}; 141 mol g^{-1} h^{-1} @ 1 A cm^{-2}), long stability of 156 h at 200 mA cm^{-2} with FE over 80%, resulting in a specific H_2O_2 yield up to 4830.43 mol g^{-1}. Besides, in the natural seawater from Bohai Sea, this catalyst exhibits a high H_2O_2 yield (14.2 mol g^{-1} h^{-1} @ 100 mA cm^{-2}) with FE over 70%, enabling it to directly synthesize H_2O_2 without the requirement of post-synthesis separation. This study also provides an alternative pathway for $2e^-$ ORR catalyst design oriented by enhancing the water dissociation kinetics.

Methods

Materials

All chemicals were utilized without further purification. $Ni(NO_3)_2{\cdot}6H_2O$ (AR, 98.0%), Co $(NO_3)_2{\cdot}6H_2O$ (AR, 98.0%), $FeCl_3{\cdot}6H_2O$ (AR, 99.0%), KOH (AR, 95.0%), HNO_3 and Na_2SO_4 (AR, 85%) were purchased from Aladdin Reagents. NaCl (GR, 99.8%) were procured from Macklin (AR Analytical reagent, GR Guaranteed reagent). Nafion (5.0 wt%) was procured from Sigma-Aldrich. Nafion-117 membrane and Pt-C (20.0 wt%) were acquired from Johnson Mattey.

Synthesis of O-CNT

The reaction flask equipped with reflux condenser, magnetic stirrer and thermometer was mounted in the preheated oil bath. Next, predetermined quantities of raw MWCNTs (2.5 g) and nitric acid (200 ml) were added into a two-necked, round-bottomed glass flask at 80 °C for 12 h. The sample was filtered on a membrane filter, washed to neutral pH, dried at 60 °C for 24 h to get about 1 g O-CNTs[47].

Synthesis of $Ni(OH)_2$/CNT

2.5 mmol $Ni(NO_3)_2{\cdot}6H_2O$ (726.963 mg) and 30 mg O-CNTs were dissolved in 30 ml deionized water. After slow addition of 10 mL 1 M KOH aqueous solution, the mixed suspension was transferred to a 50 ml polytetrafluoroethylene inner liner, and reacted at 180 °C for 12 h. The solid obtained was washed with a large amount of deionized water, and dried at 60 °C overnight to get about 229 mg $Ni(OH)_2$/CNT.

Synthesis of NiO/CNT

2.5 mmol $Ni(NO_3)_2{\cdot}6H_2O$ (726.963 mg) and 30 mg O-CNTs were dissolved in 30 ml deionized water. After slow addition of 10 mL 1 M KOH aqueous solution, the mixed suspension was transferred to a 50 ml polytetrafluoroethylene inner liner, and reacted at 180 °C for 12 h. The solid obtained was washed with a large amount of deionized water, and dried at 60 °C overnight to get **1**; To synthesize the NiO/CNT, the obtained **1** was placed in the middle of the quartz crucible and calcined at 500 °C with a heat rate of 5 °C/min under flowing Ar and maintained at this temperature for 2 h in a muffle furnace and NiO/CNT was obtained.

Synthesis of $Ni(OH)_2$

2.5 mmol $Ni(NO_3)_2{\cdot}6H_2O$ (726.963 mg) was dissolved 30 ml deionized water. After quick addition of 10 mL 1 M KOH aqueous solution, the mixed suspension was transferred to a 50 ml polytetrafluoroethylene inner liner, and reacted at 180 °C for 12 h. The green solid obtained was washed with a large amount of deionized water, and dried at 60 °C overnight to get $Ni(OH)_2$.

Characterization

Hitachi S-4800 scanning electron microscopy (SEM), Hitachi Jem-2100F transmission electron microscopy (TEM) were used for the morphological and structural characterizations. The composition of the samples and elemental mapping was analyzed by energy-dispersive X-ray spectroscope (EDX) attached to the TEM instrument. Bruker D8 Advanced X-ray diffraction (XRD) with Cu Ka radiation (k = 1.5418 Å) was used for analyzing the crystal structure of as-prepared materials. X-ray photoelectron spectroscopy (XPS, Thermo Scientific ESCALAB 250Xi) with Al Ka X-rays was utilized to investigate the chemical state of the elements of the as-prepared products. XAFS spectra were measured at the beamline BL14W1 station of the Shanghai Synchrotron Radiation Facility. The Ni *K*-edge XANES data were recorded in transmission mode with Ni foil, standard $Ni(OH)_2$ as references. The EXAFS raw data were background-subtracted, normalized, and Fourier transformed by standard procedures using the Athena and Artemis implemented in the IFEFFIT software packages. The existence of O-vacancy was analyzed by EPR spectra (Bruker EMXplus).

Electrochemical tests

The electrochemical measurements were conducted at room temperature (~25 °C). All electrochemical tests were conducted on the CHI 760E workstation with an RRDE-3A Rotating Ring Disk Electrode (RRDE) Apparatus (ALS Co, Ltd, Japan), using a typical three-electrode system at room temperature. An RRDE loaded with catalysts was employed as the working electrode. An Ag/AgCl electrode and a carbon rod were used as the reference electrode and counter electrode, respectively. 1 mg of catalyst was dispersed in a mixture of 1 mL of 700 μL deionized water, 200 μL isopropanol and 100 μL PTFE (0.2 wt%) solution to form the ink (1 mg/mL). After that, 20 μL of catalyst (catalyst loading: 0.808 mg cm^{-2}) was drop-casted on the disk electrode (area: 0.2475 cm^2), and the H_2O_2 produced during the reaction was measured by the ring electrode (area: 0.1866 cm^2). Cyclic voltammetry (CV) was performed in 0 to 1.0 V vs. RHE for ~10 cycles before linear scanning voltammetry (LSV) testing to activate the catalysts with a scan rate of 10 mV s^{-1} and rotation rate of 1600 revolutions per minute (rpm). The scan voltage range of LSV in 0.9 wt% NaCl and 0.1 M Na_2SO_4 is from 0.6 to −0.35 V *vs.* RHE, in 3.6 wt% NaCl is from 0.6 to −1.1 V *vs.* RHE. the scan voltage range in 0.1 M KOH, 0.1 M KOH + 3.6 wt% NaCl, seawater + 0.1 M KOH is from 0.9 to 0 V vs. RHE. Ring electrode potential was set at 1.2 V vs. RHE to detect the amount of generated H_2O_2. At this voltage, only H_2O_2 formed at the disk electrode is oxidized without affecting the ORR current at the ring electrode. The H_2O_2 selectivity (H_2O_2%) and transfer electron number (n) of the catalysts were calculated based on the current of ring (I_R, mA) and disk (I_D, mA):

$$H_2O_2\% = \frac{2I_R/N}{I_D + (I_R/N)} \times 100\% \tag{1}$$

$$n = 4 \times \frac{I_D}{I_D + (I_R/N)} \tag{2}$$

Where *N* is the collection efficiency, which was calibrated by the reversible $[Fe(CN)_6]^{4-}/[Fe(CN)_6]^{3-}$ redox couple, $N = 0.37$

CER was measured by using single electrolyzer, in which Ru/Ir-coated Ti mesh (commercial) was used as the working electrode, Ag/AgCl and platinum plate as the reference electrode and counter electrode. The H_2O_2 reduction performance was analyzed in the Ar-saturated 3.6 wt% NaCl solution with 10 mM H_2O_2.

H_2O_2 yield measurements

H_2O_2 generated by continuous ORR electrolysis in the electrolyte can be accumulated and quantified. Electrochemical synthesis of H_2O_2 and quantification of H_2O_2 production rate were performed in a flow cell. 20 μL catalysts ink of 5 mg/mL (5.0 mg catalyst powder in the mixture of 700 uL of deionized water, 200 μL isopropanol and 100 μL of 0.2 wt% PTFE solution) was dripped on the gas-diffusion layer (GDL, SGL-39BB), which was used as the cathode electrode with a catalyst loading of 0.1 mg cm^{-2}, Ru/Ir-coated Ti mesh (commercial, 2 × 2 cm^2), and Ag/AgCl electrode were used as the counter electrode and reference electrode, respectively. Nafion117 membrane (thickness: 183 μm) was used to separate the cathode from the anode chamber. The membrane was treated by protonating it in a 5 wt% aqueous H_2O_2 solution at 80 °C for 1 h then boiling it in a 5 wt% H_2SO_4 at 80 °C for 1 h. Next, washing it several times with deionized water, then it was soaked in deionized water. The H_2O_2 concentration in the final electrolyte was determined by the potassium titanium oxalate colorimetric method. Standard solutions were prepared with 100 μL H_2O_2 (variable concentrations), 0.5 mL 0.05 M potassium titanium oxalate, 0.5 mL 3 M H_2SO_4, and 3.9 mL DI water. Absorbance at 400 nm (UV-vis) was fitted with H_2O_2 concentration to generate the calibration curve[48]. The LSV test at different potentials from 0.6 to −1.4 V vs. RHE and the i-t test at 200 mA cm^{-2} current densities. The FE of H_2O_2 generation in the flow cell was calculated as follows:

$$FE(\%) = \frac{2cVF}{Q} \times 100\% \tag{3}$$

Where c and V are the H_2O_2 concentration calculated and the volume of the electrolyte of the cathode, F is the Faraday constant and Q is the total charge passed.

In situ ATR-SEIRAS measurements

In situ ATR-SEIRAS was performed on a Nicolet iS50 spectrometer equipped with a VeeMax III (PIKE technologies) accessory. The electrochemical test was conducted in a custom-made three-electrode electrochemical single cell. A Pt wire (commercial) and a saturated Ag/AgCl were used as the counter and reference electrodes, respectively. 0.1 mg electrocatalyst was sprayed on a Si wafer coated with Au layer. This Si wafer was used to load the catalysts and served as the working electrode. The in-siut ATR-SEIRAS spectrum were recorded by varying the potential stepwise from 0.5 V to 0 V vs. RHE in O_2-saturated 3.6 wt% NaCl and run time was 60 s.

Density functional theory (DFT) calculations

Spin-polarized DFT calculations were performed with the Vienna Ab Initio Simulation Package (VASP)[49]. The exchange-correlation interaction was described using Perdew-Burke-Ernzerhof functional[50]. The Projector Augmented Wave potentials were used to treat electronic cores[51]. The plane-wave cutoff energy of geometry optimizations was set to 450 eV. All the slab were separated with a 15 Å vacuum in z-direction. The k-points of 3 × 2 × 1 Gamma-centered grids were used during the optimization. The convergence of atomic relaxations was applied with the max force of 0.02 eV $Å^{-1}$.

The computational hydrogen electrode (CHE) model[52] was applied to calculate free energies of absorbed species:

$$G = E + ZPE - TS \tag{4}$$

Where E is the total energy computed by DFT optimization. ZPE and TS represent zero-point energy correction and entropy correction.

The climbing-image nudged elastic band (CI-NEB)[53] was used to calculate kinetic barriers of chemical reaction process, convergence thresholds of energy and force were 1×10^{-4} eV and 0.05 eV $Å^{-1}$, respectively. The implicit solvent effect was applied by using VASPsol with the linearized Poisson-Boltzman model[54]. The Debye screening length was adjusted to 3.0 Å, and the relative permittivity was set to 78.4. In this work, we employed the python code developed by Duan's group for GC-DFT calculations. Different voltage was applied through the change of electrons using the counter-charge distribution[55–57], The potential of the electrode was calculated by correlating the work function (W_f) of the system with the experimental W_f of the standard hydrogen electrode (SHE). The potential−dependent electrochemical energy can be expressed as[58,59]

$$E = E_{vasp} + e\phi_{\mathrm{elyte}}\Delta_q - \left(\mu_e + e\phi_{\mathrm{elyte}}\right)\Delta_q = E_{vasp} - E_F\Delta_q \tag{5}$$

Where E_{vasp} is the DFT energy determined by VASPsol, ϕ_{elyte} signifies the inherent electrostatic potential within the bulk electrolyte. E_F represents Fermi energy, also coincides with the electron chemical potential μ_e, Δ_q represents the extra numbers of electrons. The relation between E_F and the corresponding electrode potential referenced to the standard hydrogen electrode scale U (V vs SHE) is formulated as:

$$U(\mathrm{V}\ vs.\ \mathrm{SHE}) = -4.6V - \left(E_F + E_{Femishift}\right)/e \tag{6}$$

Where $E_{Femishift}$ is the Femi energy shift given by VASPsol.

Molecular dynamics (MD) simulations

Molecular dynamics (MD) simulations were carried out by utilizing the Large-scale Atomic/Molecular Massively Parallel Simulator (LAMMPS)[60] for the purpose of exploring the ion distributions on the catalyst surfaces of $Ni(OH)_2$, Ni, and NiO. During the entirety of the simulations, the system was run at a temperature of 300 K within the NVT ensemble for a period of 4 ns to achieve equilibrium. A variable electric field in the Z direction was applied to each atom, with the selected voltage values being 0, 0.1, and 1 V $Å^{-1}$ respectively. Periodic boundary conditions were applied within the horizontal plane. To simulate the electrolyte employed in the experiment (3.6 wt% NaCl), the solvent model consisted of 1500 H_2O molecules, 28 Na^+ ions, and 28 Cl^- ions. The interatomic interactions between the catalysts and H_2O as well as various ions were described by means of Coulomb and Lennard-Jones potentials. The corresponding parameters for Na^+ and Cl^- were developed by In Suk Joung and Thomas E Cheatham[61]. The interaction among H_2O molecules was depicted by the SPC/E model[62]. The IFF interaction parameters of $Ni(OH)_2$, Ni, and NiO were referred to following previous reports[63]. Furthermore, the detailed simulation models of both $Ni(OH)_2$, Ni, and NiO catalysts are shown in Supplementary Figs. 2 and 3. The cutoff distance was set to 10 Å for both of the aforesaid potentials, and the time step was 1 fs. All the configurations were visualized via the use of OVITO software[64].

Statistics & reproducibility

No data were excluded from the analyses.

Data availability

All data generated in this study are provided in the Supplementary Information/Source Date file. Source data are provided with this paper.

References

1. Mase, K., Yoneda, M., Yamada, Y. & Fukuzumi, S. Seawater usable for production and consumption of hydrogen peroxide as a solar fuel. *Nat. Commun.* **7**, 11470 (2016).
2. Sun, L., Jin, X., Su, T., Fisher, A. C. & Wang, X. Conjugated nickel phthalocyanine derivatives for heterogeneous electrocatalytic H_2O_2 synthesis. *Adv. Mater.* **36**, e2306336 (2023).
3. Cao, P. et al. Metal single-site catalyst design for electrocatalytic production of hydrogen peroxide at industrial−relevant currents. *Nat. Commun.* **14**, 172 (2023).
4. Zhang, E. et al. Engineering the local atomic environments of indium single-atom catalysts for efficient electrochemical production of hydrogen peroxide. *Angew. Chem. Int. Ed.* **61**, e202117347 (2022).
5. Kim, H. W. et al. Efficient hydrogen peroxide generation using reduced graphene oxide–based oxygen reduction electrocatalysts. *Nat. Catal.* **1**, 282–290 (2018).
6. Zhi, Q. et al. Dithiine-linked metalphthalocyanine framework with undulated layers for highly efficient and stable H_2O_2 electroproduction. *Nat. Commun.* **15**, 678 (2024).
7. Yan, M. et al. Sb_2S_3-templated synthesis of sulfur-doped Sb-N-C with hierarchical architecture and high metal loading for H_2O_2 electrosynthesis. *Nat. Commun.* **14**, 368 (2023).
8. Yu, L. et al. Non-noble metal-nitride based electrocatalysts for high-performance alkaline seawater electrolysis. *Nat. Commun.* **10**, 5106 (2019).
9. Liang, Q. et al. Efficient osmosis-powered production of green hydrogen. *Nat. Sustain.* **7**, 628–639 (2024).
10. Lim, T. et al. Atomically dispersed Pt-N_4 sites as efficient and selective electrocatalysts for the chlorine evolution reaction. *Nat. Commun.* **11**, 412 (2020).
11. Yao, Y. et al. Single atom Ru monolithic electrode for efficient chlorine evolution and nitrate reduction. *Angew. Chem. Int. Ed.* **61**, e202208215 (2022).

12. Cao, P. et al. Highly efficient acidic electrosynthesis of hydrogen peroxide at industrial-level current densities promoted by alkali metal cations. *Angew. Chem. Int. Ed.* **63**, e202406452 (2024).
13. Tian, X., Zhao, P. & Sheng, W. Hydrogen evolution and oxidation: mechanistic studies and material advances. *Adv. Mater.* **31**, e1808066 (2019).
14. Murray, A. T., Voskian, S., Schreier, M., Hatton, T. A. & Surendranath, Y. Electrosynthesis of hydrogen peroxide by phase-transfer catalysis. *Joule* **3**, 2942–2954 (2019).
15. Yu, D. et al. Electronic structure modulation of iron sites with fluorine coordination enables ultra-effective H_2O_2 activation. *Nat. Commun.* **15**, 2241 (2024).
16. Kim, C. et al. Concurrent oxygen reduction and water oxidation at high ionic strength for scalable electrosynthesis of hydrogen peroxide. *Nat. Commun.* **14**, 5822 (2023).
17. Qin, C. et al. Dual donor-acceptor covalent organic frameworks for hydrogen peroxide photosynthesis. *Nat. Commun.* **14**, 5238 (2023).
18. Duan, X. et al. Dynamic chloride ion adsorption on single iridium atom boosts seawater oxidation catalysis. *Nat. Commun.* **15**, 1973 (2024).
19. Zhang, X. et al. Electrochemical oxygen reduction to hydrogen peroxide at practical rates in strong acidic media. *Nat Commun.* **13**, 2880 (2022).
20. Wang, B. et al. Structure inheritance strategy from MOF to edge-enriched NiFe-LDH array for enhanced oxygen evolution reaction. *Appl. Catal. B* **298**, 120580 (2021).
21. Zhang, Z. et al. Engineering ultrafine NiFe-LDH into self-supporting nanosheets: separation-and-reunion strategy to expose additional edge sites for oxygen evolution. *Small* **17**, 2103785 (2021).
22. Zhou, B. et al. Platinum modulates redox properties and 5-Hydroxymethylfurfural adsorption kinetics of $Ni(OH)_2$ for biomass upgrading. *Angew. Chem. Int. Ed.* **60**, 22908–22914 (2021).
23. Zhou, K. L. et al. Platinum single-atom catalyst coupled with transition metal/metal oxide heterostructure for accelerating alkaline hydrogen evolution reaction. *Nat. Commun.* **12**, 3783 (2021).
24. Wang, Y. et al. Charge-polarized selenium vacancy in nickel diselenide enabling efficient and stable electrocatalytic conversion of oxygen to hydrogen peroxide. *Adv. Sci.* **10**, 2205347 (2022).
25. Raza, M. H. et al. Gas sensing of NiO-SCCNT core-shell heterostructures: optimization by radial modulation of the hole-accumulation layer. *Adv. Funct. Mater.* **30**, 1906874 (2019).
26. Guo, X., Kong, R.-M., Zhang, X., Du, H. & Qu, F. $Ni(OH)_2$ nanoparticles embedded in conductive microrod array: an efficient and durable electrocatalyst for alkaline oxygen evolution reaction. *ACS Catal.* **8**, 651–655 (2017).
27. Lee, B.-H. et al. Supramolecular tuning of supported metal phthalocyanine catalysts for hydrogen peroxide electrosynthesis. *Nat. Catal.* **6**, 234–243 (2023).
28. Chen, J. et al. Reversible hydrogen spillover in Ru-WO_{3-x} enhances hydrogen evolution activity in neutral pH water splitting. *Nat. Commun.* **13**, 5382 (2022).
29. Zhang, Y. et al. Metastable hexagonal phase SnO_2 nanoribbons with active edge sites for efficient hydrogen peroxide electrosynthesis in neutral media. *Angew. Chem. Int. Ed.* **62**, e202218924 (2023).
30. Wan, C. et al. Amorphous nickel hydroxide shell tailors local chemical environment on platinum surface for alkaline hydrogen evolution reaction. *Nat. Mater.* **22**, 1022–1029 (2023).
31. Peng, W. et al. Facilitating two-electron oxygen reduction with pyrrolic nitrogen sites for electrochemical hydrogen peroxide production. *Nat. Commun.* **14**, 4430 (2023).
32. De Luna, P. et al. What would it take for renewably powered electrosynthesis to displace petrochemical processes? *Science* **364**, eaav3506 (2019).
33. Du, J. et al. CoIn dual-atom catalyst for hydrogen peroxide production via oxygen reduction reaction in acid. *Nat. Commun.* **14**, 4766 (2023).
34. Jung, E. et al. Atomic-level tuning of Co-N-C catalyst for high-performance electrochemical H_2O_2 production. *Nat. Mater.* **19**, 436–442 (2020).
35. Guo, J. et al. Direct seawater electrolysis by adjusting the local reaction environment of a catalyst. *Nat. Energy* **8**, 264–272 (2023).
36. Zhang, X. et al. Developing Ni single-atom sites in carbon nitride for efficient photocatalytic H_2O_2 production. *Nat. Commun.* **14**, 7115 (2023).
37. Tang, C. et al. Tailoring acidic oxygen reduction selectivity on single-atom catalysts via modification of first and second coordination spheres. *J. Am. Chem. Soc.* **143**, 7819–7827 (2021).
38. Jing, L. et al. Unveiling favorable microenvironment on porous doped carbon nanosheets for superior H_2O_2 electrosynthesis in neutral media. *Adv. Energy Mater.* **14**, 2304418 (2024).
39. Tse, E. C. et al. Proton transfer dynamics control the mechanism of O_2 reduction by a non-precious metal electrocatalyst. *Nat. Mater.* **15**, 754–759 (2016).
40. Li, Y. et al. Enhancing local CO_2 adsorption by L-histidine incorporation for selective formate production over the wide potential window. *Angew. Chem. Int. Ed.* **62**, e202313522 (2023).
41. Dong, Z. et al. Cerium dioxide as an electron buffer to stabilize iridium for efficient water electrolysis. *Adv. Funct. Mater.* **34**, 2400809 (2024).
42. Nayak, S., McPherson, I. J. & Vincent, K. A. Adsorbed intermediates in oxygen reduction on platinum nanoparticles observed by In situ IR spectroscopy. *Angew. Chem. Int. Ed.* **57**, 12855–12858 (2018).
43. Huang, S. et al. Well-defined N_3C_1-anchored single-metal-sites for oxygen reduction reaction. *Angew. Chem. Int. Ed.* **63**, e202314833 (2024).
44. Liu, H. et al. High-performance alkaline seawater electrolysis with anomalous chloride promoted oxygen evolution reaction. *Angew. Chem. Int. Ed.* **62**, e202311674 (2023).
45. Zhao, S. et al. Constructing regulable supports via non-stoichiometric engineering to stabilize ruthenium nanoparticles for enhanced pH-universal water splitting. *Nat Commun.* **15**, 2728 (2024).
46. Kunimatsu, K., Yoda, T., Tryk, D. A., Uchida, H. & Watanabe, M. In situ ATR-FTIR study of oxygen reduction at the Pt/Nafion interface. *Phys. Chem. Chem. Phys.* **12**, 621–629 (2010).
47. Rosca, I. D., Watari, F., Uo, M. & Akasaka, T. Oxidation of multiwalled carbon nanotubes by nitric acid. *Carbon* **43**, 3124–3131 (2005).
48. Liu, W. et al. Efficient and economic H2O2 electrosynthesis via two-electron oxygen reduction reaction enabled by dynamically reconstructed Mn(*OH)-N3O-C motif and coupled alcohol oxidation.*J. Energy Chem.* **108**, 675–684 (2025).
49. Kresse, G. & Furthmuller, J. Efficient iterative schemes for ab initio total-energy calculations using a plane-wave basis set. *Phys. Rev. B* **54**, 11169–11186 (1996).
50. Perdew, J. P., Burke, K. & Ernzerhof, M. Generalized gradient approximation made simple. *Phys. Rev. Lett.* **77**, 3865–3868 (1996).
51. Blöchl, P. E. Projector augmented-wave method. *Phys. Rev. B* **50**, 17953–17979 (1994).
52. Nørskov, J. K. et al. Origin of the overpotential for oxygen reduction at a fuel-cell cathode. *J. Phys. Chem. B* **108**, 17886–17892 (2004).
53. Henkelman, G., Uberuaga, B. P. & Jónsson, H. A climbing image nudged elastic band method for finding saddle points and minimum energy paths. *J. Chem. Phys.* **113**, 9901–9904 (2000).
54. Mathew, K., Sundararaman, R., Letchworth-Weaver, K., Arias, T. A. & Hennig, R. G. Implicit solvation model for density-functional study of nanocrystal surfaces and reaction pathways. *J. Chem. Phys.* **140**, 084106 (2014).

55. Chan, K. & Norskov, J. K. Electrochemical barriers made simple. *J. Phys. Chem. Lett.* **6**, 2663–2668 (2015).
56. Duan, Z. & Xiao, P. Simulation of potential-dependent activation energies in electrocatalysis: mechanism of O-O bond formation on RuO_2. *J. Phys. Chem. C* **125**, 15243–15250 (2021).
57. Huang, Y., Nielsen, R. J. & Goddard, W. A. 3rd. Reaction mechanism for the hydrogen evolution reaction on the basal plane sulfur vacancy site of MoS_2 using grand canonical potential kinetics. *J. Am. Chem. Soc.* **140**, 16773–16782 (2018).
58. Mathew, K., Kolluru, V. S. C., Mula, S., Steinmann, S. N. & Hennig, R. G. Implicit self-consistent electrolyte model in plane-wave density-functional theory. *J. Chem. Phys.* **151**, 234101 (2019).
59. Liu, J. C., Luo, F. & Li, J. Electrochemical potential-driven shift of frontier orbitals in M-N-C single-atom catalysts leading to inverted adsorption energies. *J. Am. Chem. Soc.* **145**, 25264–25273 (2023).
60. Thompson, A. P. et al. LAMMPS-a flexible simulation tool for particle-based materials modeling at the atomic, meso, and continuum scales. *Comput. Phys. Commun.* **271**, 108171 (2022).
61. Canongia Lopes, J. N., Deschamps, J. & Pádua, A. A. H. Modeling Ionic liquids using a systematic all-atom force field. *J. Phys. Chem. B* **108**, 2038–2047 (2004).
62. Joung, I. S. & Cheatham, T. E. III Determination of alkali and halide monovalent Ion parameters for use in explicitly solvated biomolecular simulations. *J. Phys. Chem. B* **112**, 9020–9041 (2008).
63. Kanhaiya, K. *Development and application of reliable models for the simulation of metals and oxides at the nanoscale*. Thesis, Univ. of Colo. (2022).
64. Stukowski, A. Visualization and analysis of atomistic simulation data with OVITO—the open visualization tool. *Model. Simul. Mater. Sci. Eng.* **18**, 015012 (2010).
65. Zhao, Q. et al. Approaching a high-rate and sustainable production of hydrogen peroxide: oxygen reduction on Co-N-C single-atom electrocatalysts in simulated seawater. *Energy Environ. Sci.* **14**, 5444–5456 (2021).
66. Zhang, C. et al. Crystal engineering enables cobalt-based metal-organic frameworks as high-performance electrocatalysts for H_2O_2 production. *J. Am. Chem. Soc.* **145**, 7791–7799 (2023).
67. Liu, L. et al. Atomically dispersed asymmetric cobalt electrocatalyst for efficient hydrogen peroxide production in neutral media. *Nat. Commun.* **15**, 4079 (2024).
68. Jing, L. et al. Efficient neutral H_2O_2 electrosynthesis from favorable reaction microenvironments via porous carbon carrier engineering. *Angew. Chem. Int. Ed.* **63**, e202403023 (2024).
69. Xia, Y. et al. Highly active and selective oxygen reduction to H_2O_2 on boron-doped carbon for high production rates. *Nat. Commun.* **12**, 4225 (2021).
70. Wang, R. et al. Structural modulation of covalent organic frameworks for efficient hydrogen peroxide electrocatalysis. *Angew. Chem. Int. Ed.* **63**, e202410417 (2024).
71. Chen, S. et al. Chemical identification of catalytically active sites on oxygen-doped carbon nanosheet to decipher the high activity for electro-synthesis hydrogen peroxide. *Angew. Chem. Int. Ed.* **60**, 16607–16614 (2021).
72. Chen, Y. et al. Oxygen functional groups regulate cobalt-porphyrin molecular electrocatalyst for acidic H_2O_2 electrosynthesis at industrial-level current. *Angew. Chem. Int. Ed.* **63**, e202407163 (2024).

Acknowledgments

This work was supported by the National Natural Science Foundation of China (No. 22379111 and 22179093 to J.L.), Key Research Project of Shenzhen (KCXFZ20240903094159005 to X.Y.) and Shenzhen General Project for Institutions of Higher Education (No. 20231127113219001 to X.Y.).

Author contributions

J.N. and Q.J. contributed equally to this work. Z.S. and J.L. designed the project. J.N. conducted the sample synthesis and characterization and electrochemical tests. Q.J. performed the DFT calculations. J.N. wrote the paper. M.Z., Z.L., W.L. and X.Y. assisted with electrochemical testing, D.Y., F.H., Y.Z., and X.Y. advised on experiments, and L.Y. provided guidance on DFT calculations. All authors reviewed the manuscript.

Competing interests

The authors declare no competing interests.

Additional information

Supplementary information The online version contains supplementary material available at https://doi.org/10.1038/s41467-025-60950-8.

Correspondence and requests for materials should be addressed to Zhiyuan Sang, Lichang Yin, Xiao Yan or Ji Liang.

Peer review information *Nature Communications* thanks Guanjie He and the other, anonymous, reviewer(s) for their contribution to the peer review of this work. A peer review file is available.

Reprints and permissions information is available at http://www.nature.com/reprints

Publisher's note Springer Nature remains neutral with regard to jurisdictional claims in published maps and institutional affiliations.

Open Access This article is licensed under a Creative Commons Attribution-NonCommercial-NoDerivatives 4.0 International License, which permits any non-commercial use, sharing, distribution and reproduction in any medium or format, as long as you give appropriate credit to the original author(s) and the source, provide a link to the Creative Commons licence, and indicate if you modified the licensed material. You do not have permission under this licence to share adapted material derived from this article or parts of it. The images or other third party material in this article are included in the article's Creative Commons licence, unless indicated otherwise in a credit line to the material. If material is not included in the article's Creative Commons licence and your intended use is not permitted by statutory regulation or exceeds the permitted use, you will need to obtain permission directly from the copyright holder. To view a copy of this licence, visit http://creativecommons.org/licenses/by-nc-nd/4.0/.

© The Author(s) 2025